Applied Catalysis B: Environmental 130–131 (2013) 293–304

Contents lists available at SciVerse ScienceDirect

Applied Catalysis B: Environmental

journal homepage: www.elsevier.com/locate/apcatb

A comparative study of different doped metal cations on the reduction, adsorption and activity of $CuO/Ce_{0.67}M_{0.33}O_2$ ($M = Zr^{4+}$, Sn^{4+}, Ti^{4+}) catalysts for NO + CO reaction

Xiaojiang Yao [a], Qiang Yu [a], Zeyang Ji [a], Yuanyuan Lv [a], Yuan Cao [a], Changjin Tang [a], Fei Gao [b,**], Lin Dong [a,b,*], Yi Chen [a]

[a] Key Laboratory of Mesoscopic Chemistry of MOE, School of Chemistry and Chemical Engineering, Nanjing University, Nanjing 210093, PR China
[b] Jiangsu Key Laboratory of Vehicle Emissions Control, Center of Modern Analysis, Nanjing University, Nanjing 210093, PR China

ARTICLE INFO

Article history:
Received 18 August 2012
Received in revised form 5 November 2012
Accepted 11 November 2012
Available online 24 November 2012

Keywords:
Ceria-based solid solution
Dopant
Electronegativity
Copper-based catalyst
NO + CO reaction

ABSTRACT

A series of ceria-based solid solutions ($Ce_{0.67}Zr_{0.33}O_2$, $Ce_{0.67}Sn_{0.33}O_2$, $Ce_{0.67}Ti_{0.33}O_2$) were synthesized by inverse co-precipitation, and then used as supports to prepare $CuO/Ce_{0.67}M_{0.33}O_2$ ($M = Zr^{4+}$, Sn^{4+}, Ti^{4+}) catalysts through wetness impregnation method. The obtained samples were investigated in detail by means of XRD, LRS, N_2-physisorption, H_2-TPR, XRF, XPS and in situ FT-IR techniques. The catalytic reduction of NO by CO as a model reaction was chosen to evaluate the catalytic performance of these samples. These results suggest that: (1) the reduction of $CuO/Ce_{0.67}Zr_{0.33}O_2$ is easier than $CuO/Ce_{0.67}Sn_{0.33}O_2$ and $CuO/Ce_{0.67}Ti_{0.33}O_2$ catalysts, which may be attributed to the difference in the electronegativity of dopant; (2) the reduced state Cu^+ is present in $CuO/Ce_{0.67}Zr_{0.33}O_2$ at ambient temperature due to the shifting of redox equilibrium ($Cu^{2+} + Ce^{3+} \leftrightarrow Cu^+ + Ce^{4+}$) to right; (3) the adsorbed NO species on $CuO/Ce_{0.67}Zr_{0.33}O_2$ are more liable to desorb/transform/decompose than those on $CuO/Ce_{0.67}Sn_{0.33}O_2$ and $CuO/Ce_{0.67}Ti_{0.33}O_2$ samples. The results of catalytic performance show that Cu^+/Cu^0 species play a key role in NO reduction by CO, and the activity is mainly related to the electronegativity of dopant, the reduction and adsorption behaviors of these catalysts. Furthermore, a possible reaction mechanism (schematic diagram) is tentatively proposed to understand this reaction.

1. Introduction

NO_x is one of the main pollutants in air pollution, which emits from stationary and mobile sources, such as coal-fired power plant and vehicle exhaust. The catalytic reduction of NO by CO is an important approach to remove this pollutant. According to some literatures, supported noble metal catalysts like Rh, Pt and Pd have attracted much attention due to their high activity and selectivity for this reaction [1–4]. However, the practical application of supported noble metal catalysts in automobile catalytic muffler is not perfect due to their scarce, high cost, low thermal stability and poor resistance to sulfur [5–8]. As a result, many efforts have been devoted to employing the potential substitute as an active component of the catalyst. Among the available options, the use of copper-based catalysts for the catalytic reduction of NO by CO is an interesting one, from the viewpoint of cost, stability, catalytic activity and selectivity [7,9–11].

In recent years, ceria has been investigated widely in the catalysis area owing to its oxygen storage capacity (OSC) associated with the formation of oxygen vacancy and facile Ce^{4+}/Ce^{3+} redox cycle [7,11–13]. However, it is well known that sintering effect often occurs when pure CeO_2 is used at high temperature, resulting in the decrease of specific surface area and OSC [14]. Many researches have been performed by incorporating foreign metal cations into the lattice of CeO_2 to restrain this effect. These metal cations mainly contain three categories: (i) M^{2+} (Ca^{2+} [15], Mg^{2+} [16]), (ii) M^{3+} (Al^{3+}, Ga^{3+}, In^{3+} [17,18]) and (iii) M^{4+} (Zr^{4+} [19,20], Hf^{4+} [21], Sn^{4+} [22,23], Ti^{4+} [10,24], Mn^{4+} [25], Pb^{4+} [26]). Recently, our lab [19] synthesized a series of $CuO/Ce_xZr_{1-x}O_2$ catalysts used for NO reduction by CO and found that the ceria-rich sample showed higher activity than zirconia-rich sample; Cao et al. [23] prepared several $CuO/Ce_xSn_{1-x}O_2$ catalysts used in low-temperature CO oxidation, and the $CuO/Ce_{0.8}Sn_{0.2}O_2$ catalyst exhibited the best catalytic performance; Jiang et al. [10] reported that $CuO/Ce_{0.3}Ti_{0.7}O_2$ catalyst had the highest activity in NO + CO reaction among the

* Corresponding author at: Key Laboratory of Mesoscopic Chemistry of MOE, School of Chemistry and Chemical Engineering, Nanjing University, Nanjing 210093, PR China. Tel.: +86 25 83592290; fax: +86 25 83317761.
** Corresponding author. Tel.: +86 25 83596545; fax: +86 25 83317761.
E-mail addresses: gaofei@nju.edu.cn (F. Gao), donglin@nju.edu.cn (L. Dong).

0926-3373/$ – see front matter © 2012 Elsevier B.V. All rights reserved.
http://dx.doi.org/10.1016/j.apcatb.2012.11.020

$CuO/Ce_xTi_{1-x}O_2$ catalysts. According to the above-mentioned literatures, we can find that the previous works are mainly focused on investigating the catalytic property of the catalyst by modulating the ratio of Ce/M. However, there are almost few reports which focus on changing the doped metal cation of $CuO/Ce_xM_{1-x}O_2$ for a comparative study.

Many researchers reported that the redox potential and ionic radius of the dopant were responsible for the catalytic performance of the doped ceria [26,27]. As is well known, both the redox potential and ionic radius are related to the electronic structure of the dopant, which can affect the ability of the doped metal cation to capture or lose electrons. Unfortunately, the redox potential and ionic radius can be influenced by other factors, such as valence [28]. However, the electronegativity can reflect the ability of the dopant to capture or lose electrons objectively [29]. Therefore, the influence of electronegativity on the catalytic performance has attracted more attention. For example, Kobayashi et al. [30] investigated the effect of basic metal additives on NO_x reduction property over Pd-based three-way catalysts, and concluded that the NO_x conversion was improved due to the additive with lower electronegativity stabilized PdO.

In the present work, ceria doped with Zr^{4+}, Sn^{4+}, Ti^{4+} are used as supports to prepare copper-based catalysts and the obtained samples have been studied systematically by means of XRD, LRS, N_2-physisorption, H_2-TPR, XRF, XPS, in situ FT-IR, and NO + CO model reaction. The study is mainly focused on: (1) understanding the influence of dopant on the structure, texture, reduction, and adsorption properties and catalytic performance of the obtained samples; (2) investigating the interaction of CO or/and NO with these catalysts by in situ FT-IR technique; (3) exploring the key factors which can affect the activity of these catalysts for NO reduction by CO significantly.

2. Materials and methods

2.1. Catalysts preparation

The $Ce_{0.67}M_{0.33}O_2$ (M = Zr^{4+}, Sn^{4+}, Ti^{4+}) solid solutions (Ce:M = 2:1 mol ratio) were prepared by inverse co-precipitation method. The requisite quantity of ammonium cerium (IV) nitrate as Ce source was dissolved in distilled water to form solution. The Zr, Sn, and Ti sources were zirconium (IV) nitrate, tin (IV) tetrachloride, and titanium (IV) tetrachloride. These precursors of M source were also added into distilled water, respectively. The above two solutions (Ce and M) were mixed together and stirred for 2 h, and then slowly added into the excess ammonia (25%) with vigorously stirring until pH = 10. The resulting solutions were kept in stirring for another 3 h, aged 24 h, and then filtered, washed several times with distilled water until no pH change (especially for $Ce_{0.67}Sn_{0.33}O_2$ and $Ce_{0.67}Ti_{0.33}O_2$, until no Cl^- which was detected by the solution of $AgNO_3$). The obtained cakes were oven dried at 110 °C for 12 h and finally calcined at 550 °C in the flowing air for 5 h. In addition, pure CeO_2 was prepared via the same procedure for comparison. These synthesized samples were CeO_2, $Ce_{0.67}Zr_{0.33}O_2$ (hereafter denoted as CZ), $Ce_{0.67}Sn_{0.33}O_2$ (hereafter denoted as CS), and $Ce_{0.67}Ti_{0.33}O_2$ (hereafter denoted as CT) supports.

The CuO/S (S = CeO_2, CZ, CS, CT) catalysts were prepared by wetness impregnation method with $Cu(NO_3)_2$ solution. The mixture was kept in stirring for 2 h and evaporated at 100 °C during the oil bath. The resulting materials were dried at 110 °C for 12 h in the oven, and then calcined at 500 °C in the flowing air for 5 h. The CuO loading amount was 0.4 mmol/g-support, and these catalysts were denoted as 04CuO/CeO_2, 04CuO/CZ, 04CuO/CS, and 04CuO/CT, respectively.

2.2. Catalysts characterization

Powder X-ray diffraction (XRD) patterns were recorded on a Philips X'pert Pro diffractometer using Ni-filtered Cu Kα radiation (λ = 0.15418 nm). The X-ray tube was operated at 40 kV and 40 mA. The intensity data were collected over a 2θ range of 10–80° with a 0.02° step size. The mean grain sizes (D_β) from the (111) plane of these samples were determined from XRD line broadening measurements using the Debye-Scherrer equation, $D_\beta = K\lambda/\beta\cos\theta$, where K is the particle shape factor, usually taken as 0.89, λ is the X-ray wavelength, β is the full-width at half maximum height (FWHM) in radians, and θ is the diffraction angle.

Laser Raman spectra (LRS) were collected on a Renishaw invia Laser Raman spectrometer using Ar^+ laser beam. The Raman spectra were recorded with an excitation wavelength of 514 nm and the laser power of 20 mW.

Textural characteristics of these supports were obtained from nitrogen adsorption at 77 K on a Micromeritics ASAP-2020 analyzer, using the BET method for the specific surface area and the BJH method for the pore distribution. Prior to each analysis, the sample was degassed under vacuum at 300 °C for 4 h.

H_2-temperature programmed reduction (H_2-TPR) experiments were performed with H_2 as a reductant in a quartz U-type reactor, and 25 mg sample was used for each measurement. Prior to the reduction, the sample was pretreated in a high purified N_2 stream at 300 °C for 1 h and then cooled to room temperature. After that, the H_2-Ar mixture (6.9% H_2 by volume) was switched on, and the TPR started from 50 °C to target temperature at a rate of 10 °C·min^{-1}. The consumption of H_2 was monitored by using a thermal conductivity detector (TCD).

X-ray fluorescence spectra (XRF) were carried out on an ARL-9800 apparatus to determine the bulk composition of these catalysts. The X-ray tube was operated at 60 kV and 20 mA. The accurate measurement mode was adopted to determine the contents of Cu, Ce, Zr, Sn and Ti elements of these catalysts.

X-ray photoelectron spectroscopy (XPS) analysis was performed on a PHI 5000 VersaProbe system, using monochromatic Al Kα radiation (1486.6 eV) operating at an accelerating power of 15 kW. Before the measurement, the sample was outgassed at room temperature in a UHV chamber (< 5×10^{-7} Pa). The sample charging effect was compensated by calibrating all binding energies (BE) with the adventitious C 1s peak at 284.6 eV. The experimental error was within ±0.1 eV.

In situ Fourier transform infrared (in situ FT-IR) spectra were recorded on a Nicolet 5700 FT-IR spectrometer equipped with a DTGS as detector working at a spectral resolution of 4 cm^{-1}, and taking 32 scans for each spectrum. The catalyst was pressed into a self-supporting wafer (about 15 mg), and mounted in a commercial controlled environment chamber (HTC-3). The wafer was pretreated with high purified N_2 at 300 °C for 1 h to remove impurities. After cooling to ambient temperature, the sample was exposed to a controlled stream of CO-Ar (10% of CO by volume) or/and NO-Ar (5% of NO by volume) at a rate of 5.0 ml·min^{-1} for 40 min to be saturated. CO or/and NO adsorption in situ FT-IR spectra were collected at various target temperatures at a rate of 10 °C·min^{-1} from room temperature to 325 °C by subtraction of the corresponding background reference.

2.3. Catalytic performance tests

The catalytic activity and selectivity of these catalysts were determined under light-off procedure in NO + CO model reaction, involving a feed steam with a fixed composition, 5% NO, 10% CO and 85% He by volume as diluents. The sample (25 mg) was pretreated in a high purified N_2 stream at 300 °C for 1 h and then cooled to room temperature, after that, the mixed gases were switched on. The

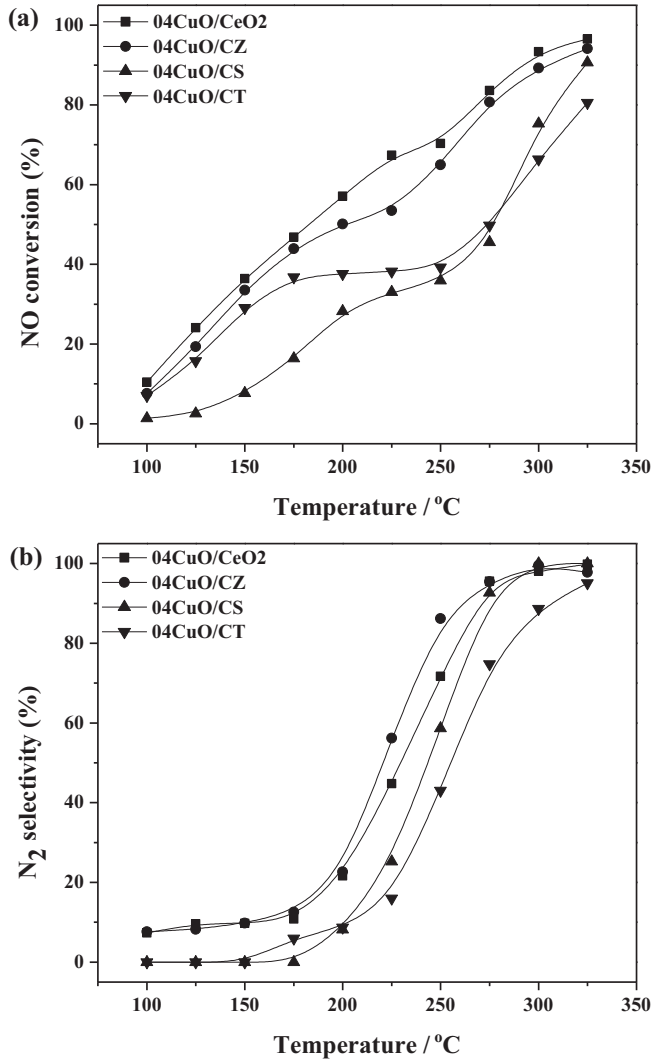

Fig. 1. The results of (a) NO conversion, and (b) N_2 selectivity over these catalysts as a function of reaction temperature.

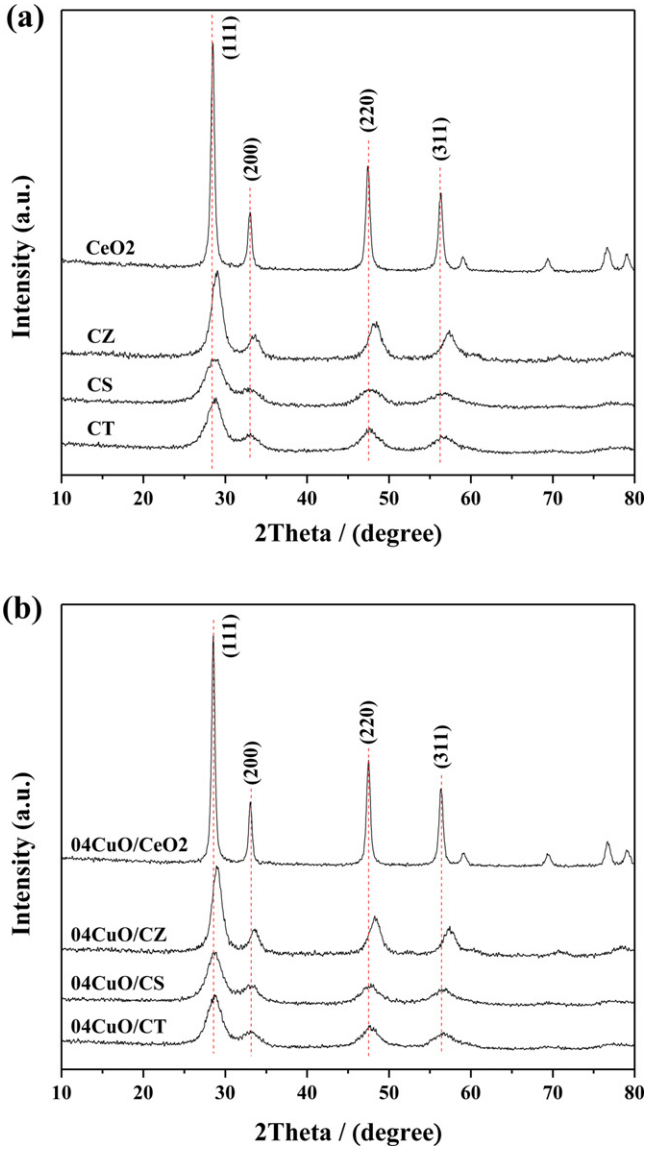

Fig. 2. The powder XRD patterns of (a) supports, and (b) catalysts.

reactions were carried out at different temperatures with a space velocity of 24,000 ml·g^{-1}·h^{-1}. Two columns (length, 1.75 m; diameter, 3 mm) and thermal conductivity detector (T = 100 °C) were used for analyzing the products. Column A with Paropak Q for separating CO_2 and N_2O, column B packed with 5A and 13X molecule sieve (40–60 M) for separating N_2, NO and CO.

3. Results and discussion

3.1. Catalytic activity/selectivity results (NO + CO model reaction)

Catalytic reduction of NO by CO was performed to evaluate the catalytic performance of these catalysts. The results of NO conversion and N_2 selectivity as a function of reaction temperature over these samples are presented in Fig. 1. We can find that when the temperature is below 200 °C, the activity of these catalysts is considerable, but the selectivity is negligible. Interestingly, the increase of the activity is very slow between 200 and 275 °C, but the selectivity is rising sharply in this temperature range for all of the catalysts. According to our previous work [8], the reason may be that the reaction of NO reduction by CO over copper-based catalysts proceeds in two sequential steps: firstly, NO is mainly converted to N_2O; secondly, N_2O is further transformed to N_2. When continue increasing the temperature up to 325 °C, both the activity and selectivity over these catalysts are close to 100%. Furthermore, it can be noticed that 04CuO/CZ shows higher activity than 04CuO/CT and 04CuO/CS, but slightly lower than 04CuO/CeO_2. Fortunately, 04CuO/CZ possesses the best selectivity among these catalysts. In order to further explore the reason for the difference of the catalytic performance, we carried out a series of characterizations over these samples, and the corresponding results were given in the following sections.

3.2. Structural characteristics (XRD and LRS)

Fig. 2 shows the XRD patterns of these samples. We can find that CZ, CS, and CT supports are in a poorly crystalline form, and only the broad diffraction lines pertained to cubic fluorite-type CeO_2 (PDF-ICDD 34-0394) can be observed. The characteristic lines attributed to ZrO_2, SnO_2, and TiO_2 are absent, and the diffraction peaks of CZ, CS, and CT shift to high angle direction slightly compared to CeO_2, which indicate that Zr^{4+}, Sn^{4+}, and Ti^{4+} have been successfully doped into the lattice of CeO_2 to form uniform solid solutions. Noted from Table 1, the grain size of CZ, CS, and CT is smaller than CeO_2, suggesting that the introduction of Zr^{4+}, Sn^{4+},

Table 1
Grain size, lattice parameter, the position and FWHM of the main Raman line, and the peak area ratio in Raman of the samples.

Samples	Grain size (nm)	Lattice parameter (Å)	Position of Raman line (cm^{-1})	FWHM of Raman line (cm^{-1})	$(A_I + A_{III})/A_{II}$
CeO_2	20.4	5.422	464	42.8	0.0368
CZ	7.8	5.321	474	109.4	0.5124
CS	3.0	5.385	455	49.2	0.3076
CT	5.1	5.384	460	44.4	0.2696
$04CuO/CeO_2$	21.1	5.418	447	48.4	0.0726
04CuO/CZ	8.8	5.320	462	113.5	0.6072
04CuO/CS	4.0	5.381	443	53.1	0.3689
04CuO/CT	5.4	5.380	445	49.4	0.3249

and Ti^{4+} inhibits the crystal growth of the cubic phase [24]. Furthermore, the lattice parameter decreases with the substitution of Ce^{4+} ($r = 0.92$ Å) by Zr^{4+} ($r = 0.80$ Å), Sn^{4+} ($r = 0.71$ Å), and Ti^{4+} ($r = 0.68$ Å) due to the lattice shrinkage and distortion [31].

After the impregnation of copper oxide species, all of the samples maintain their original crystal structure with no additional diffraction peaks for crystalline CuO, indicating that copper oxide species are highly dispersed and/or present as small clusters which are difficult to be detected due to the limitation of XRD. The data (Table 1) show that the grain size of CeO_2, CZ, CS, and CT increases slightly after the introduction of copper oxide species. The phenomenon may be due to the second calcination of these samples after the impregnation of copper oxide species. In addition, according to our previous work [32], there are some cubic vacant sites on the surface of these supports. Table 1 displays that the lattice parameter of CeO_2, CZ, CS and CT decreases slightly after the addition of copper oxide species, probably due to the incorporation of monolayer copper ($r_{Cu}{}^{2+} = 0.72$ Å) into the surface/subsurface layers of these supports to occupy the vacant sites [19].

It is well known that Raman spectrum of pure CeO_2 is characterized by a strong peak at *ca.* 462 cm^{-1} due to the F_{2g} Raman active mode of the fluorite structure [33]. In addition, it also exhibits a weak band at *ca.* 260 cm^{-1} and a shoulder at *ca.* 600 cm^{-1}, which are linked to oxygen vacancies in the CeO_2 lattice [34]. Fig. 3 illustrates the Raman spectra of the supports and catalysts, respectively. All of the supports show a prominent band at 455–474 cm^{-1} (labeled II), a weak band at 261–300 cm^{-1} (labeled I) and a shoulder at 600–629 cm^{-1} (labeled III). However, the Raman lines assigned to MO_2 (M = Zr^{4+}, Sn^{4+}, Ti^{4+}) are not observed. Interestingly, the main band shifts slightly to higher or lower wavenumbers with the incorporation of Zr^{4+}, Sn^{4+}, and Ti^{4+} into the lattice of CeO_2 (Table 1), which is in agreement with XRD measurements.

For the catalysts, the Raman lines of CuO are absent in all of the samples, indicating that the copper oxide species are in the forms of highly dispersed and clustered states on the surface of the supports. Moreover, the main band of these catalysts is red shifting to 443–462 cm^{-1}, comparing with their supports. This can be attributed to the following two reasons. One is that the existence of interaction between support and active species according to the literature [18]. The other reason may be that the incorporation of monolayer copper ($r_{Cu}{}^{2+} = 0.72$ Å) into the surface/subsurface layers of these supports, which is in line with XRD results. Since the bands I and III are related to oxygen vacancies, and the band II is the main band of these samples, the area ratio of $(A_I + A_{III})/A_{II}$ can reflect the concentration of oxygen vacancies. As a result, we can notice from Table 1 that the concentration of oxygen vacancies and the FWHM of these catalysts increased by the impregnation of copper oxide species.

3.3. Textural characterization (N_2-physisorption)

The N_2 adsorption-desorption isothermal plots and the corresponding BJH pore size distribution curves of CeO_2, CZ, CS, and CT supports are shown in Fig. 4. The isotherms of these supports are of classical type IV as defined by IUPAC [35], which is characteristic of mesoporous materials due to the textural of inter-particle mesoporosity. A well-defined H2-type hysteresis loop with a sloping adsorption branch and a relatively steep desorption branch is observed at high relative pressure range (P/P_0) for every sample. This H2-type of the hysteresis loop is typical for wormhole-like mesostructure and interstice mesoporous structure formed by nanoparticle assembly [20]. Furthermore, the pore size distribution curves of these samples determined by the BJH method from

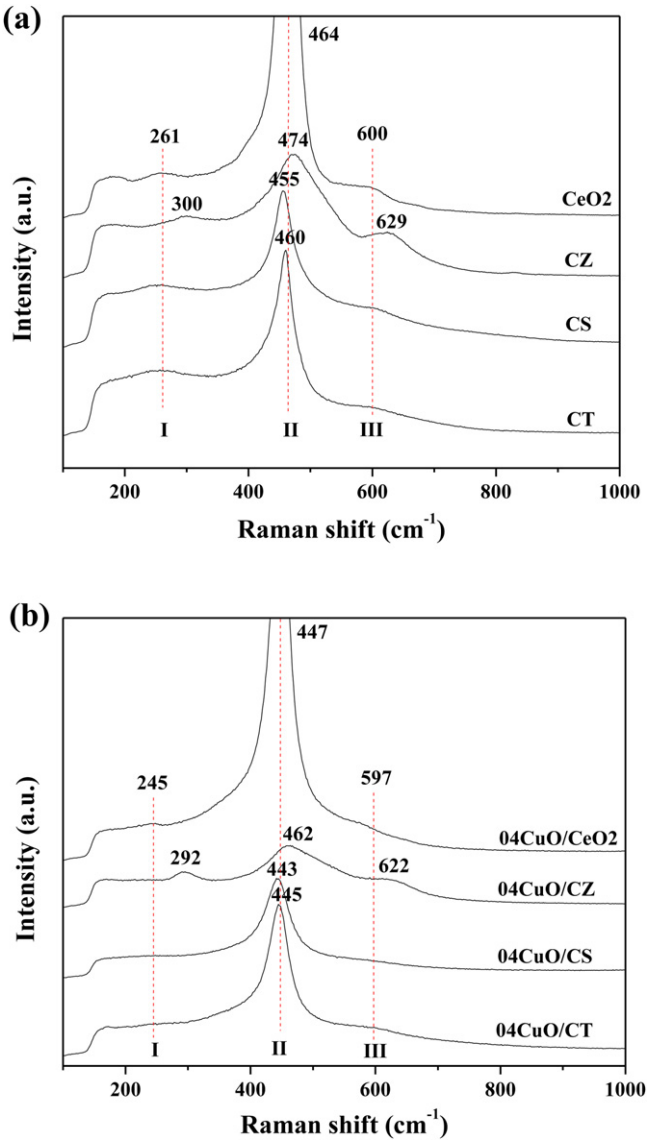

Fig. 3. The Raman spectra of (a) supports, and (b) catalysts.

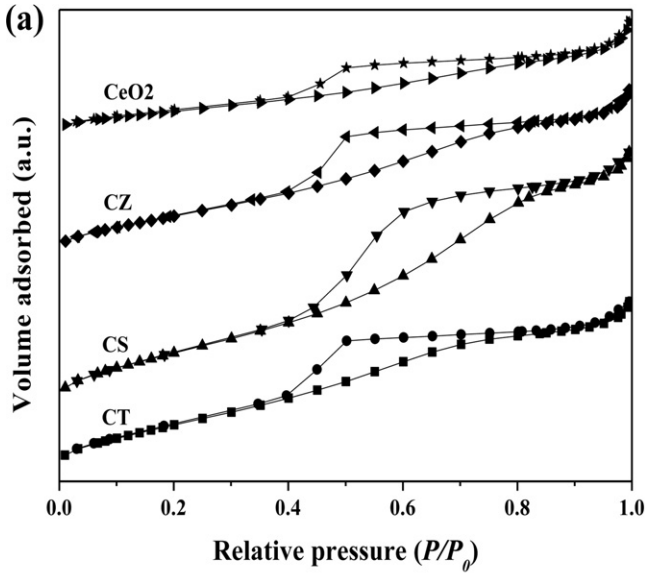

Fig. 4. The (a) N_2 adsorption-desorption isotherms, and (b) BJH pore distribution curves of CeO_2, CZ, CS, and CT supports.

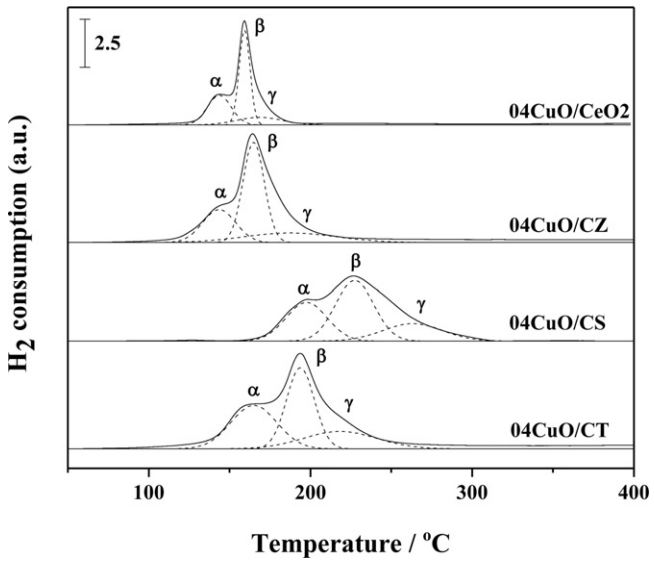

Fig. 5. H_2-TPR profiles of these catalysts.

adsorption branch of the corresponding isotherm exhibit one single narrow peak centered at 4.18–6.33 nm, indicating that these supports possess uniform mesopore size distributions.

The textural data of CeO_2, CZ, CS, and CT supports are listed in Table 2. Compared with pure CeO_2, when the foreign metal cations are doped into the lattice of CeO_2 (formed CZ, CS, and CT solid solutions), both the specific surface area and pore volume are increased, which is beneficial to the dispersion of active component. These changes may be related to the particle size of the samples to some extent. In other words, the incorporation of Zr^{4+}, Sn^{4+}, and Ti^{4+} into the lattice of CeO_2 can improve the texture property effectively. In addition, in order to explore the thermal stability, all of the four supports were calcined at 800 °C for 5 h in flowing air, and then, BET measurements were carried out, and the specific surface areas were also summarized in Table 2. Compared with pure CeO_2, the degree of sintering (i.e., $(S_{BET}(550)–S_{BET}(800))/S_{BET}(550)$) is smaller when Zr^{4+}, Sn^{4+}, and Ti^{4+} incorporate into the lattice of CeO_2. It indicates that the ability of anti-sintering of CeO_2 is enhanced with the introduction of these foreign metal cations.

3.4. Reduction properties of the catalysts (H_2-TPR)

H_2-TPR tests were performed to study the reducibility of these catalysts. Fig. 5 shows that the shape of these TPR profiles is very similar, and all of them exhibit three reduction peaks (labeled as α, β, and γ). The two peaks at low temperature region (α and β) are mainly attributed to the stepwise reduction of surface dispersed copper oxide species, i.e., $Cu^{2+} \rightarrow Cu^{+}$ and $Cu^{+} \rightarrow Cu^{0}$ [6,32,36,37], while the other one at high temperature region (γ) may be mainly assigned to the reduction of clustered state CuO [38]. Therefore, the H_2-TPR results are well in agreement with the XRD observations.

The information of these reduction peaks are summarized in Table 3. The temperature of the reduction peaks of the four catalysts increases in the sequence of 04CuO/CeO_2 < 04CuO/CZ < 04CuO/CT < 04CuO/CS due to the difference of interaction between copper oxide species and the corresponding support. In detail, since the electronegativity of these elements contained in the obtained catalysts is presented via the following order: Ce < Zr < Ti < Cu < Sn (Table 4), the electrons can be captured by Cu^{2+} in these

Table 2
The textural properties of CeO_2, CZ, CS, and CT supports.

Samples	BET surface area ($m^2\ g^{-1}$)	Pore volume ($cm^3\ g^{-1}$)	Average pore diameter (nm)	$(S_{BET}(550)–S_{BET}(800))/S_{BET}(550)$
CeO_2	35.9	0.055	6.33	/
CZ	66.8	0.073	4.74	/
CS	87.6	0.112	6.25	/
CT	76.4	0.076	4.18	/
CeO_2-800	2.2	/	/	0.9387
CZ-800	26.4	/	/	0.6048
CS-800	23.3	/	/	0.7340
CT-800	22.5	/	/	0.7055

Table 3
The temperature of the reduction peak, the actual and theoretical H_2 consumption of these catalysts.

Samples	T_α/°C	T_β/°C	T_γ/°C	The actual H_2 consumption (μmol/g)	The theoretical H_2 consumption (μmol/g)
04CuO/CeO_2	144	159	171	524	388
04CuO/CZ	145	164	191	985	388
04CuO/CS	198	227	265	1379	388
04CuO/CT	166	194	222	1256	388

Table 4
The electronegativity (χ) and the gradient of electronegativity between Cu and M (M = Ce, Zr, Sn, Ti).

Element	Electronegativity (χ)	$\chi_{Cu} - \chi_{M\ (M=Ce, Zr, Sn, Ti)}$
Ce	1.10	0.80
Zr	1.33	0.57
Sn	1.96	−0.06
Ti	1.54	0.36
Cu	1.90	/

catalysts through the Cu-O-M (M = Ce, Zr, Ti) link except 04CuO/CS (the electrons donate to Sn^{4+}, so the reduction of CuO in 04CuO/CS is very difficult). Furthermore, the ability of Cu^{2+} to capture electrons weakens with the decreasing gradient of electronegativity ($\chi_{Cu}-\chi_M$). As a result, the easy degree of reduction for these catalysts decreases in accordance with the order: 04CuO/CeO_2 > 04CuO/CZ > 04CuO/CT > 04CuO/CS. Moreover, it is noteworthy that the actual H_2 consumption of these catalysts is higher than the value for complete reduction of CuO component to Cu^0 (i.e., the theoretical H_2 consumption). This excess hydrogen uptake should be due to the possibility of partial reduction of the supports through donation of mobile oxygen to copper oxide species [16], indicating that these reduction peaks of the four catalysts should include the surface layer reduction of the corresponding support.

3.5. Bulk and Surface analysis of the catalysts (XRF and XPS)

The bulk composition of these catalysts was determined by XRF, and the results are summarized in Table 5. From this table, we can find that the actual contents of these metal cations are very close to the nominal values (within the parentheses) for each catalyst, indicating that the losses of these metal cations in the preparation process are negligible. XPS was adopted to study the surface composition and elemental oxidation states of the catalysts. The XPS spectra of Ce 3d, Cu 2p, O 1s, Zr 3d, Sn 3d, and Ti 2p of the catalysts are displayed in Fig. 6. For the XPS spectrum of Ce 3d, the absolute distinction between $3d^94f^2V^{n-1}$ and $3d^94f^2V^{n-2}$ final states for Ce^{3+} (ν^0, u^0) and Ce^{4+} (ν, u) could not be resolved due to the complex electronic structure [39]. Therefore, for all of the catalysts, the high-resolution spectrum of Ce 3d is numerically fitted with eight components with the assignment defined in Fig. 6a. The bands labeled ν' and u' represent $3d^{10}4f^1$ initial electronic state corresponding to Ce^{3+}, while the bands labeled ν''' and u''' represent $3d^{10}4f^0$ state of Ce^{4+} [40]. As a result, the chemical valence of cerium on the surface of these catalysts is mainly in a +4 oxidation state, and a small quantity of Ce^{3+} co-exists.

Fig. 6b exhibits the XPS spectrum of Cu 2p for all of the catalysts. It can be seen from this figure, for 04CuO/CeO_2, 04CuO/CZ, and 04CuO/CT catalysts, most of Cu is in a +2 oxidation state and a small amount in a +1 oxidation state, located at 934.0 eV and 932.0 eV, respectively [7,20]. The reason for the generation of Cu^+ may be that the electronegativity of Cu is bigger than that of Ce, Zr, and Ti (Table 4), so the electron can donate to Cu^{2+}. Furthermore, the generation of Cu^+ together with the observation of Ce^{3+} species is indicative of the redox equilibrium ($Cu^{2+} + Ce^{3+} \leftrightarrow Cu^+ + Ce^{4+}$) shifting to right, which is claimed to be the source of a synergistic effect on catalytic performance [19]. However, for 04CuO/CS catalyst, the binding energy of Cu $2p_{3/2}$ is only at 934.0 eV, indicating that all of Cu is in a +2 oxidation state. The possible reason for the absence of Cu^+ is that the electronegativity of Cu is smaller than Sn (Table 4), as a result, the redox equilibrium ($Cu^{2+} + Ce^{3+} \leftrightarrow Cu^+ + Ce^{4+}$) cannot establish, replacing by the other redox equilibrium ($Sn^{4+} + 2Ce^{3+} \leftrightarrow Sn^{2+} + 2Ce^{4+}$), which is supported by the results of Fig. 6a and Fig. 6d. In addition, Baidya et al. [22] reported that the Sn^{4+}/Sn^{2+} species can generate in $Ce_{1-x}Sn_xO_2$ easily, which further confirmed our speculation.

The high-resolution spectrum for the O 1s ionization features of these catalysts is numerically fitted with two components representing the primary O 1s ionization feature and chemically shifted O 1s feature from chemisorbed surface species, which is presented in Fig. 6c. The primary band O′ (529.2 eV) is attributed to the O 1s ionization for oxygen of the metal oxides [39], while the shoulder O″ (531.1 eV) shifting to higher binding energy is the result of chemisorbed oxygen [27]. We can notice that the O 1s ionization features for all of the catalysts are very similar (Fig. 6c).

In addition, the narrow scan spectra of Zr 3d, Sn 3d, and Ti 2p are exhibited in Fig. 6d. The binding energy of Zr $3d_{5/2}$ (181.9 eV) in 04CuO/CZ is consistent with ZrO_2 (181.9 eV), indicating that Zr is mainly in a +4 oxidation state [41]. Considering the XPS spectrum of Sn 3d, we can find that most of Sn is in a +4 oxidation state and a small quantity in a +2 oxidation state, because that the binding energy of Sn $3d_{5/2}$ (486.0 eV) in 04CuO/CS is lower than that in SnO_2 (486.2 eV) but higher than that in SnO (485.6 eV) [42,43], suggesting that the Sn^{4+}/Sn^{2+} species can generate in 04CuO/CS easily, which is in agreement with the result of Baidya et al. [22]. The appearance of Sn^{2+} is reasonable, we know that the electronegativity of Sn is larger than Ce and Cu (Table 4), so the electrons will donate to Sn^{4+} during 04CuO/CS, resulting in the redox equilibrium ($Sn^{4+} + 2Ce^{3+} \leftrightarrow Sn^{2+} + 2Ce^{4+}$) shifting to right. For 04CuO/CT, the binding energy of Ti $2p_{3/2}$ is 458.2 eV which coincides with TiO_2 (458.3 eV), indicating that Ti is mainly in a +4 oxidation state [44].

Table 5
The bulk and surface composition of these catalysts (M = Zr, Sn, Ti).

Sample	Atomic concentration							Atomic ratio				
	XRF (bulk)			XPS (surface)				XRF (bulk)		XPS (surface)		
	Cu (at.%)	Ce (at.%)	M (at.%)	Cu (at.%)	Ce (at.%)	M (at.%)	O (at.%)	Ce/M	Cu/(Ce + M)	Ce/M	Cu/(Ce + M)	O/(Cu + Ce + M)
04CuO/CeO_2	2.36 (2.19)	31.76 (31.87)	/	4.55	25.71	/	69.74	/	0.074 (0.069)	/	0.18	2.30
04CuO/CZ	2.13 (1.99)	21.51 (21.34)	10.40 (10.67)	3.74	16.67	9.70	69.89	2.07 (2.00)	0.067 (0.062)	1.72	0.14	2.32
04CuO/CS	2.27 (2.11)	21.56 (21.29)	10.26 (10.64)	3.20	15.93	11.38	69.49	2.10 (2.00)	0.071 (0.066)	1.40	0.12	2.28
04CuO/CT	2.02 (1.81)	21.35 (21.42)	10.63 (10.71)	2.80	18.42	7.16	71.62	2.01 (2.00)	0.063 (0.056)	2.57	0.11	2.52

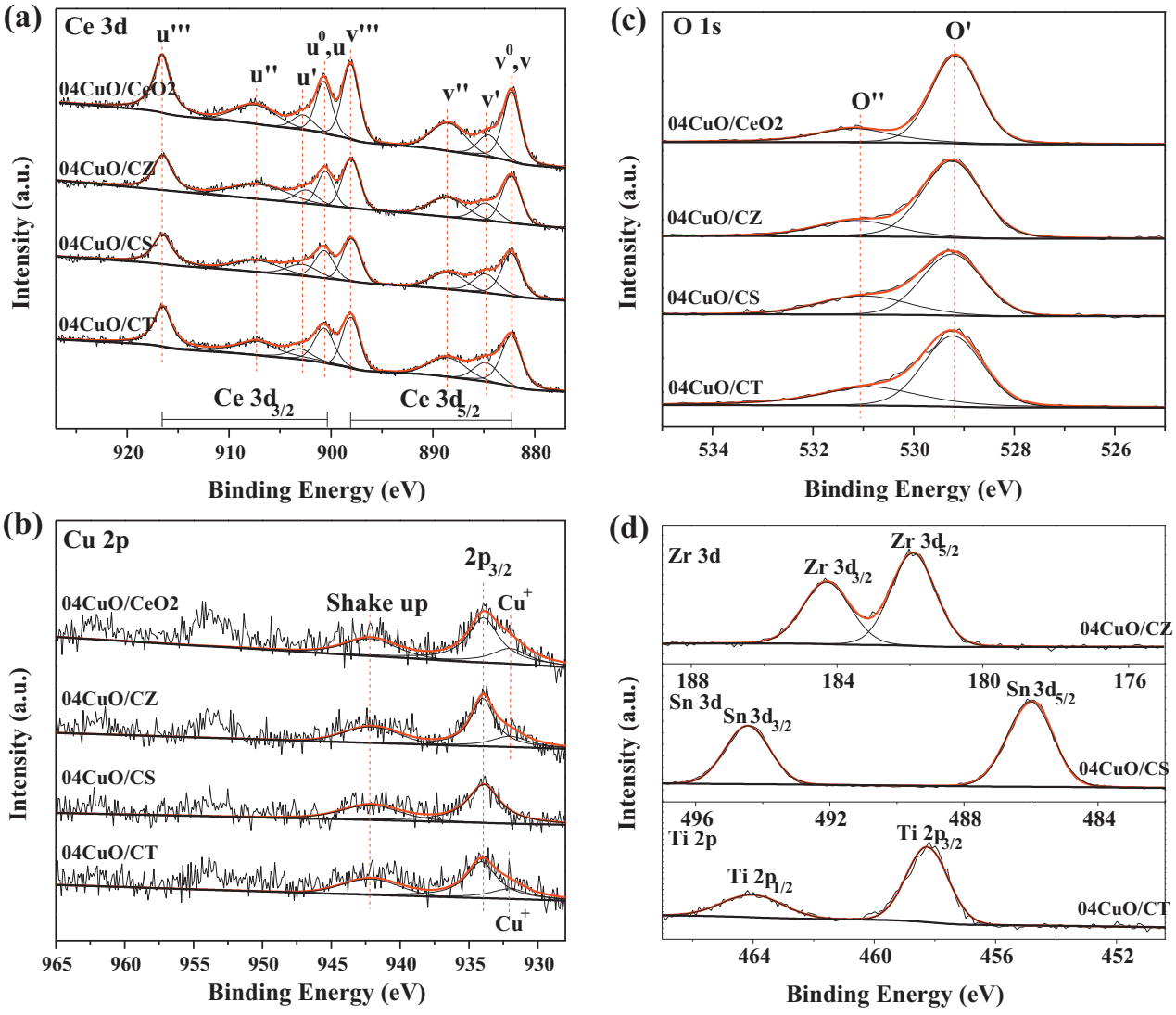

Fig. 6. XPS spectra (Ce 3d, Cu 2p, O 1s, Zr 3d, Sn 3d, and Ti 2p) of the catalysts.

The surface atomic concentration and atomic ratio of these catalysts obtained from XPS analysis are also listed in Table 5. The surface copper atomic concentration decreases in the sequence of 04CuO/CeO_2 > 04CuO/CZ > 04CuO/CS > 04CuO/CT. Simultaneously, the surface atomic concentration of copper is larger than the bulk atomic concentration for every sample, indicating that most copper species exist on the surface of these catalysts. In addition, the surface Ce/M (M = Zr, Sn) atomic ratio is a little lower than the bulk atomic ratio determined by XRF measurement (Table 5), which suggests that a small amount of Zr and Sn migrates to the surface. However, a spot of Ce is enriched on the surface of 04CuO/CT. Table 5 also shows that the surface Cu/(Ce + M) atomic ratio over the four catalysts appears to be in the similar level except 04CuO/CeO_2. Furthermore, the surface O/(Cu + Ce + M) atomic ratio over these catalysts is higher than the nominal ratio (1.97) of the fully oxidized surface, the excess surface oxygen is attributed to the adsorbed layer of water and C-O species [39].

3.6. CO or/and NO interaction with the catalysts (in situ FT-IR)

The results of CO adsorption in situ FT-IR of the catalysts are presented in Fig. 7. As reported previously, for the adsorption of CO on CuO/$Ce_xZr_{1-x}O_2$ catalysts, the band at 2113 cm^{-1} is assigned to copper carbonyl (Cu^+-CO) species on the surface of the catalysts [7,19]. The similar band can be observed in 04CuO/CeO_2, 04CuO/CZ, and 04CuO/CT catalysts at room temperature, indicating the presence of Cu^+. However, Cu^+-CO species is not detected in 04CuO/CS catalyst at room temperature, suggesting that Cu^+ is absent in 04CuO/CS catalyst at this temperature, which is in agreement with XPS results. Our previous work [45] demonstrated that Cu^+/Cu^0 species are conducive to the improvement of the catalytic performance of NO reduction by CO. Thus, the evolution of Cu^+-CO species as a function of temperature is plotted in Fig. 8. All of the curves exhibit a similar trend. Firstly, the intensity of Cu^+-CO species increases with the increasing temperature due to the reduction of Cu^{2+} to Cu^+. And then, it decreases and disappears with further raising temperature, owing to the reduction of Cu^+ to Cu^0. Therefore, we can conclude that the easy degree of the formation of Cu^+/Cu^0 species is presented via the following order: 04CuO/CeO_2 > 04CuO/CZ > 04CuO/CT > 04CuO/CS.

Fig. 9 shows the in situ FT-IR spectra of NO interaction with the catalysts. Our previous work [8] compared the interaction of NO molecules with $Ce_{0.67}Zr_{0.33}O_2$ support and 0.33CuO/$Ce_{0.67}Zr_{0.33}O_2$ catalyst by in situ FT-IR technique, and found that NO molecules interacted with the dispersed copper oxide species preferentially, thus formed several kinds of nitrate or nitrite-like species, which was supported by the results of Runduo Zhang and his co-workers [7]. Simultaneously, we also noticed that the NO adsorption in situ

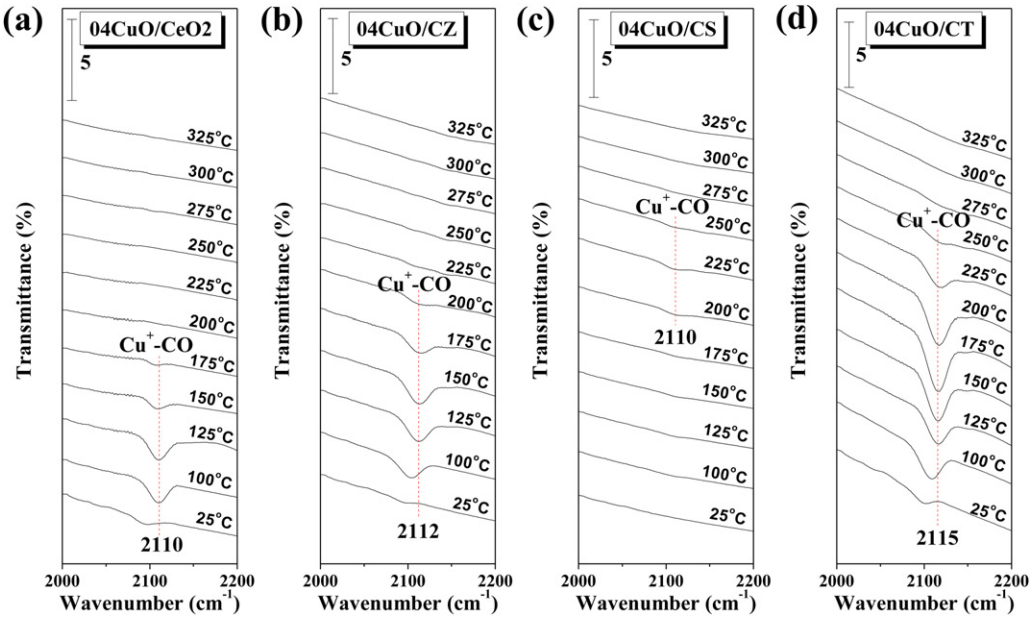

Fig. 7. In situ FT-IR spectra of CO interaction with the catalysts from 25 to 325 °C: (a) 04CuO/CeO_2, (b) 04CuO/CZ, (c) 04CuO/CS, and (d) 04CuO/CT.

FT-IR result of 0.4CuO/CeO_2 catalyst was the same with that of 0.4CuO/$Ce_{0.67}Zr_{0.33}O_2$ catalyst [46], which further demonstrated that NO molecules can interact with the dispersed copper oxide species preferentially. Interestingly, it can be seen from Fig. 9 that the adsorbed NO species exhibit their vibration bands in the similar wavenumber positions over these CuO/$Ce_{0.67}M_{0.33}O_2$ (M = Zr^{4+}, Sn^{4+}, Ti^{4+}) catalysts, which supports our previous conclusion effectively. According to some literatures [8,46–49], for some supported copper-based catalysts, bridging bidentate nitrate exhibits a remarkable NO_2 symmetric vibration band at 997–1001 cm^{-1}, and a N = O stretching model at 1626–1629 cm^{-1}. Chelating bidentate nitrate shows two bands at 1219–1223 cm^{-1} and 1564 cm^{-1}. Linear nitrite has the NO_2 asymmetric vibration band at 1269–1273 cm^{-1}. Monodentate nitrate gives two bands at 1296–1300 cm^{-1} and 1488–1506 cm^{-1}. Bridging monodentate nitrate displays a band at 1595 cm^{-1}. In addition, physical adsorbed NO species also gives a band at 1749 cm^{-1}. In the present work, with regard to 04CuO/CZ catalyst, a series of bands are observed in the 950–1800 cm^{-1} region. With the increase of temperature, linear nitrite, monodentate nitrate, bridging monodentate nitrate, and physical adsorbed NO species disappear gradually. When the temperature is up to 250 °C, a new band appears at 1564 cm^{-1}, which is assigned to chelating bidentate nitrate. Raising the temperature up to 325 °C practically leads to decrease of the bands at 1001, 1626, 1223, and 1564 cm^{-1} for bridging bidentate nitrate and chelating bidentate nitrate (but it is difficult to be completely desorbed). The situation of 04CuO/CeO_2 is similar to 04CuO/CZ. However, for 04CuO/CS and 04CuO/CT catalysts, the band for bridging monodentate nitrate does not disappear up to 325 °C, furthermore, the decrease of the bands for bridging bidentate nitrate is not obviously. Therefore, the adsorption/desorption behavior of 04CuO/CeO_2 and 04CuO/CZ is better than 04CuO/CS and 04CuO/CT catalysts. The possible reason is that when NO molecules are adsorbed on the surface of the catalyst, there will be a kind of electronic interaction that the back-donation of the d-electron from the copper cation to an antibonding orbital of NO, the effect is weakening the N-O bond of NO [50]. Because the electronegativity of these elements contained in the obtained catalysts is presented via the following order: Ce < Zr < Ti < Cu < Sn (Table 4), the electrons can be captured by Cu^{2+} in these catalysts through the Cu-O-M (M = Ce, Zr, Ti) link except 04CuO/CS (the electrons donate to Sn^{4+}). In addition, the ability of Cu^{2+} to capture electrons weakens with the decreasing gradient of electronegativity ($\chi_{Cu}-\chi_M$). In other words, the easy degree of the electrons donating to Cu^{2+} for these catalysts decreases in accordance with the order: 04CuO/CeO_2 > 04CuO/CZ > 04CuO/CT > 04CuO/CS. Furthermore, the more electrons around Cu^{2+} are conducive to the back-donation of the d-electron from the copper cation to an antibonding orbital of NO and further weaken the N-O bond of NO, which can promote the enhancement of the catalytic performance.

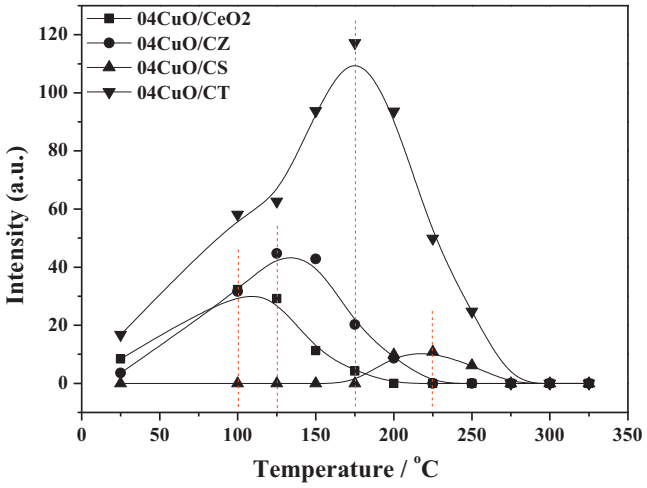

Fig. 8. Integrated intensity of CO adsorption in situ FT-IR spectra for copper carbonyl over the catalysts as a function of temperature.

In order to further approach the surface reaction mechanism, CO and NO co-adsorption in situ FT-IR spectra were recorded under the simulating reaction conditions, as shown in Fig. 10. Taking 04CuO/CZ as an example, it should be noted that neither carbonates nor Cu^+-CO species can be detected below 150 °C, indicating that NO preferentially adsorbs on the surface of the catalyst and covers the active sites, as a result, the adsorption of CO is inhibited. In this situation, the free gas CO can react with the adsorbed NO

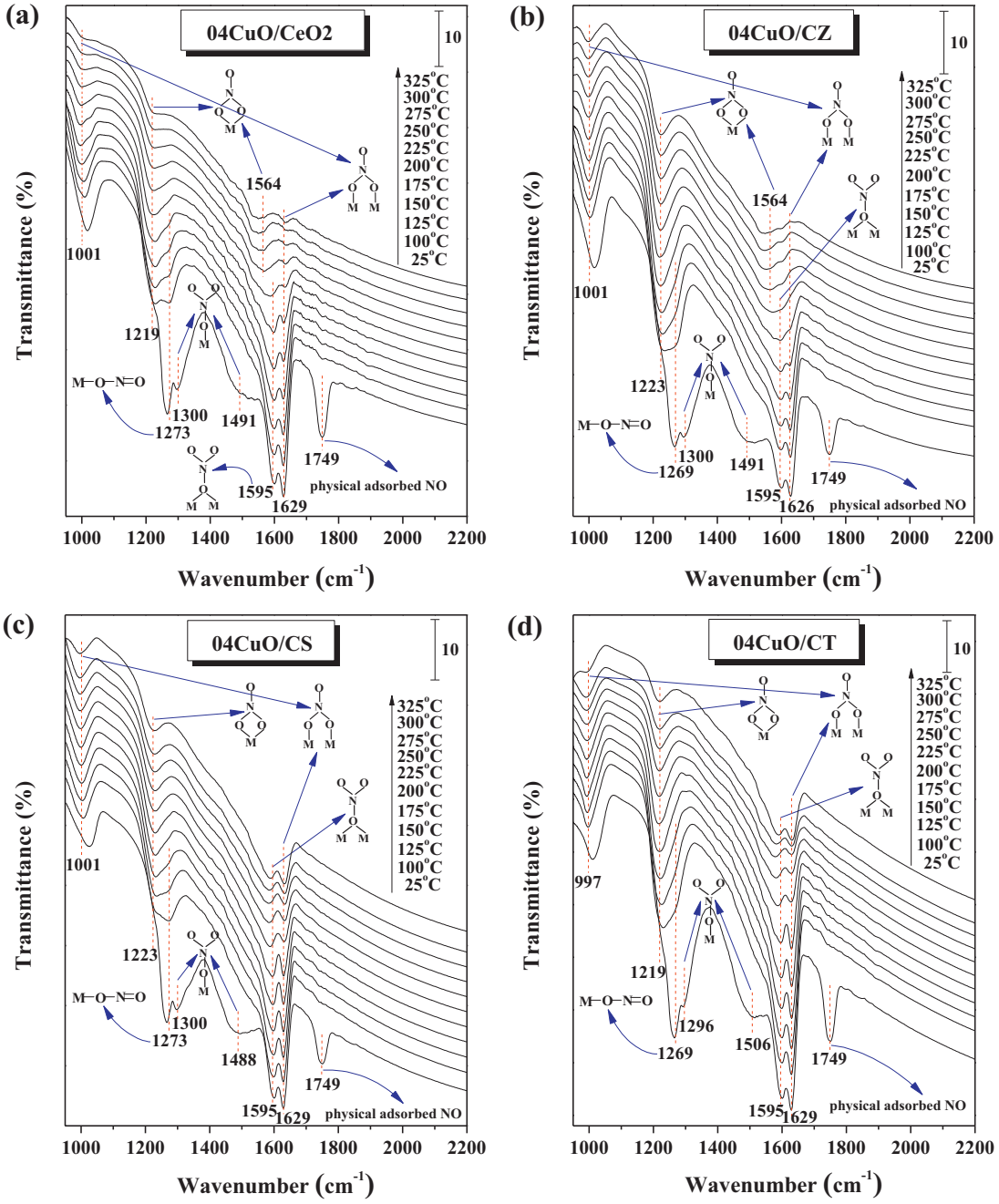

Fig. 9. In situ FT-IR results of NO interaction with the catalysts from 25 to 325 °C, the models of these adsorbed NO species were displayed in the figure: (a) 04CuO/CeO_2, (b) 04CuO/CZ, (c) 04CuO/CS, and (d) 04CuO/CT.

species slowly. Moreover, the band for CO_2 (2360 cm^{-1}) is very weak, suggesting that the reaction activity may be very low. With the temperature increasing to 150 °C, the adsorbed NO species disappears due to desorption, decomposition and reaction with the free gas CO. Therefore, the active sites of the catalyst are exposed, which can be adsorbed by CO. It is noteworthy that, the carbonates and Cu^+-CO species are observed when the temperature is up to 150 °C, indicating that CO have been adsorbed on the surface of the catalyst. Under this condition, the reaction may take place between the adsorbed CO species and the free gas NO. Interestingly, the intensity of the band for CO_2 (2360 cm^{-1}) increases significantly at 150 °C, suggesting that the reaction activity may be enhanced. Furthermore, Cu^+ can be reduced to Cu^0 by CO with further increasing temperature, which is helpful for the improvement of catalytic performance [45]. Subsequently, the same results can be found over 04CuO/CeO_2 catalyst. However, the adsorbed NO species of 04CuO/CS and 04CuO/CT catalysts disappear completely at higher temperature 200 °C and 175 °C, respectively, indicating that their catalytic performance is inferior to 04CuO/CeO_2 and 04CuO/CZ. Moreover, according to the literatures [51–53], we can find that the reaction mechanism of NO reduction by CO over noble metal catalysts (Pt, Rh, and Pt-Rh) has been investigated widely in the past decades, and a Langmuir-Hinshelwood (L-H) mechanism is recognized for these reaction systems. However, the investigation of the mechanism of this reaction on transition metal oxide catalysts is very lacking and controversial. Our previous work

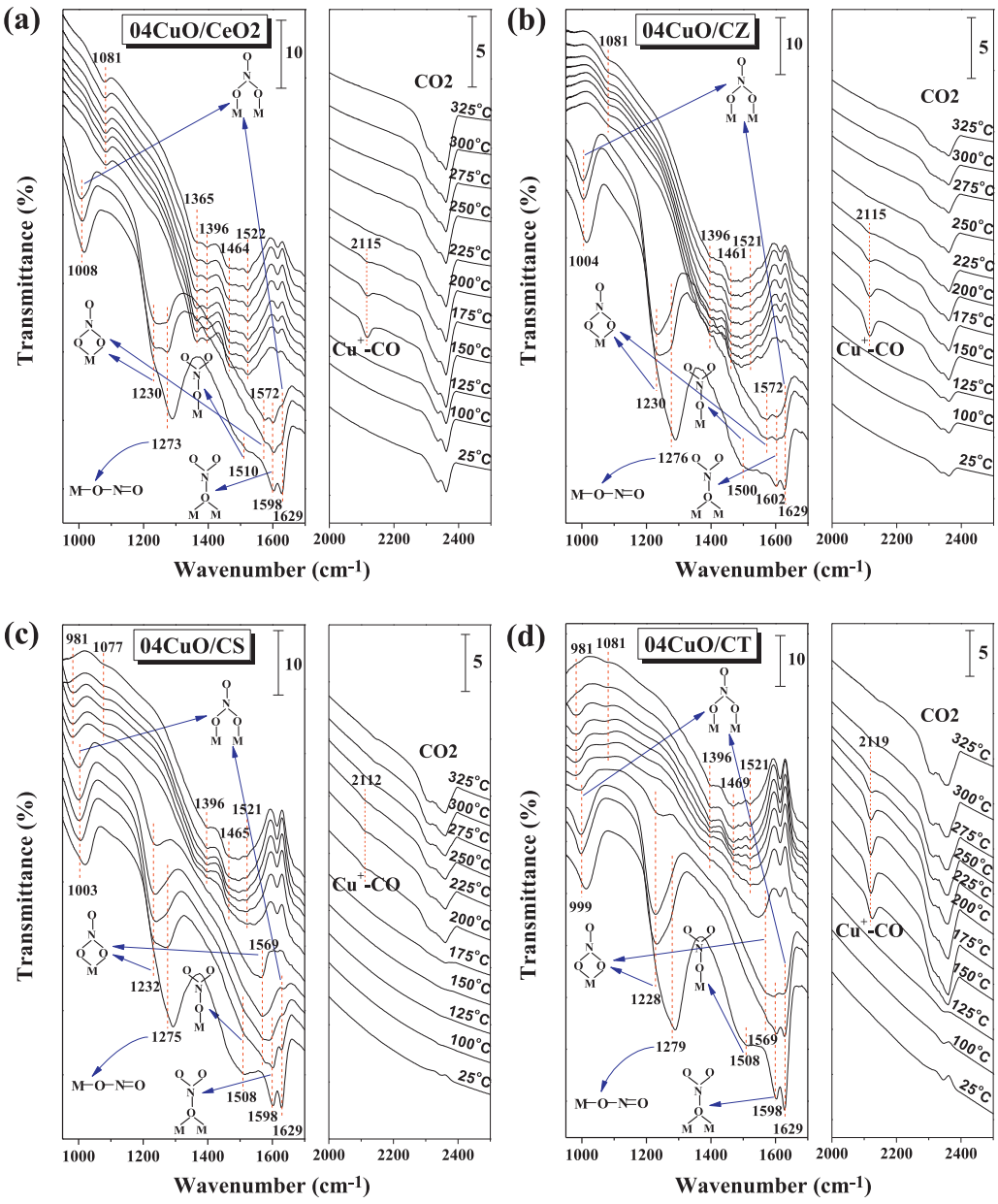

Fig. 10. In situ FT-IR results of CO and NO co-interaction with the catalysts from 25 to 325 °C, the models of these adsorbed NO species were displayed in the figure: (a) 04CuO/CeO_2, (b) 04CuO/CZ, (c) 04CuO/CS, and (d) 04CuO/CT.

[54] researched the influence of CO-pretreatment on the catalytic performance of NO reduction by CO over the supported binary metal oxides CuO-Mn_2O_3/γ-Al_2O_3 catalyst, and found that NO preferentially adsorbed on Mn^{2+} and CO on Cu^+ during the in situ FT-IR measurements, which suggested a Langmuir-Hinshelwood (L-H) mechanism due to two types of active sites (Mn^{2+} and Cu^+). While Taniike and Tada [55,56] investigated the reaction mechanism of NO reduction by CO on the supported unitary component Co^{2+}-ensemble/γ-Al_2O_3 catalyst through density functional theory (DFT) calculation and in situ FT-IR characterization, the obtained researching results indicated an Eley-Rideal (E-R) mechanism for this catalytic system. In the present work, the results of CO and NO co-adsorption in situ FT-IR show that: at low temperature (< 150 °C), only NO species can be adsorbed on the surface of these catalysts; at high temperature (>150 °C), only absorbed CO species can be observed on these catalysts surface. In other words, the reaction of NO reduction by CO over these supported unitary metal oxide CuO/$Ce_{0.67}M_{0.33}O_2$ (M = Zr^{4+}, Sn^{4+}, Ti^{4+}) catalysts is mainly taking place between adsorbed species and gaseous molecules during the whole range of reaction temperature, indicating an Eley-Rideal (E-R) mechanism, which is in accordance with the results of Taniike and Tada [55,56].

3.7. Relationship between catalytic performance and catalysts properties

Why is the catalytic performance of these catalysts different? In order to understand this question clearly, we attempt to correlate the activity with the above-mentioned characterizations, and the relationship between NO conversion (at 250 °C) and structural/textural/reducible/electronic properties is plotted in Fig. 11. As far as we know, for some important catalytic reactions, the increase of the specific surface area of support is beneficial to the dispersion of active species, which can lead the activity to increase; the activity enhances with decreasing the grain size of catalysts; the quantity of oxygen vacancy is proportional to the activity; in

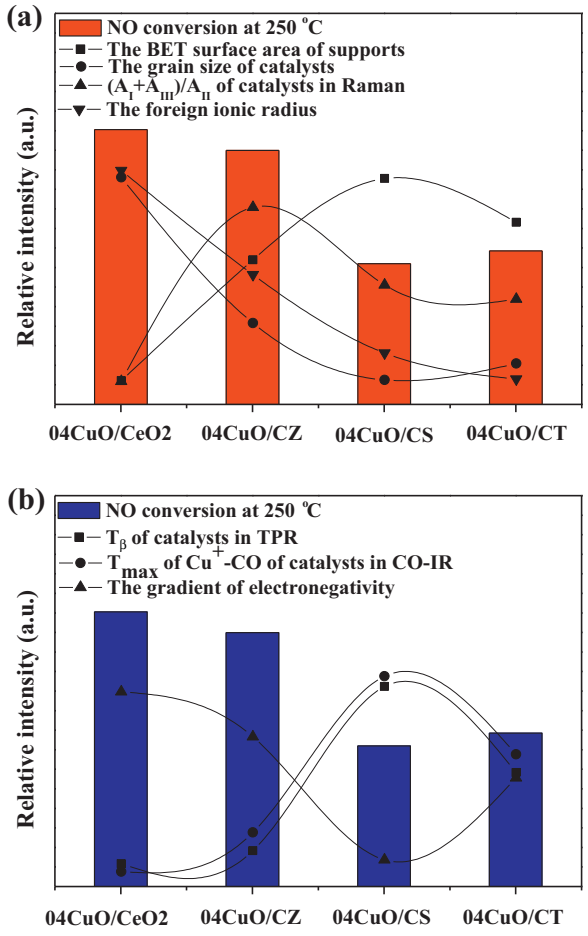

Fig. 11. The relationship between the catalytic activity of NO reduction by CO (at 250 °C) and (a) structural/textural, (b) reducible/electronic properties.

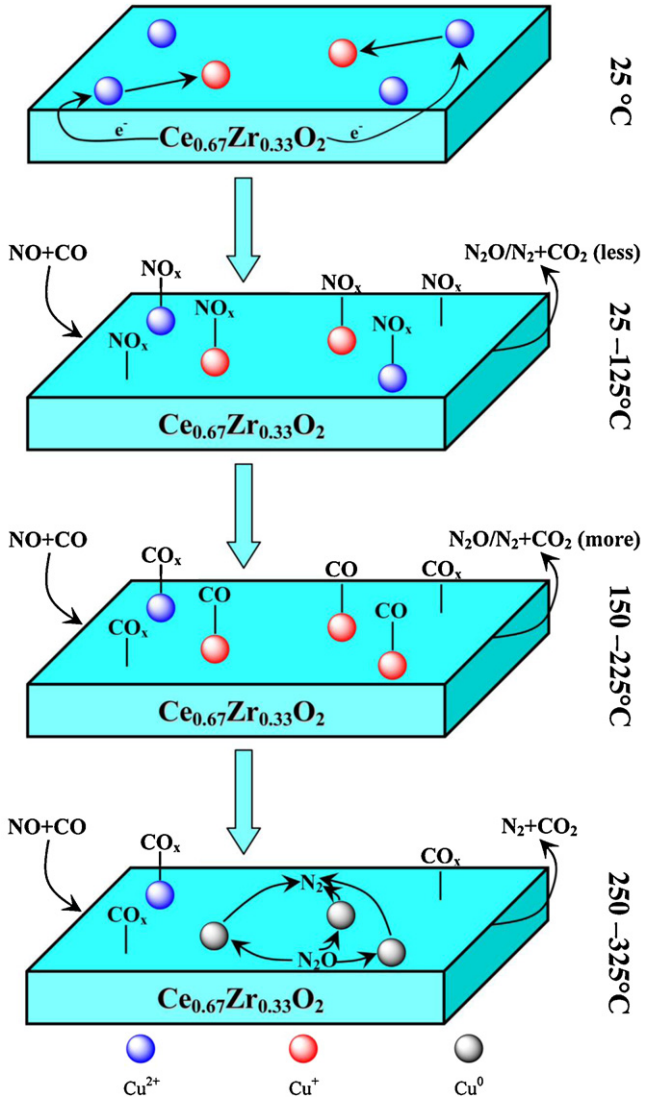

Fig. 12. Possible reaction mechanism (schematic diagram) of NO reduction by CO over 04CuO/CZ catalyst.

the situation of foreign metal cation doped into CeO_2, the smaller the foreign ionic radius, the larger the space in which oxygen atom can move, which tends to improve the activity. However, it can be noted from Fig. 11a, these properties are in contradiction with the activity. Since the activity cannot relate to the structural and textural properties very well, we take reducible and electronic properties into account. Our previous work [45] demonstrated that Cu^+/Cu^0 species are conducive to the improvement of the catalytic performance for the catalytic reduction of NO by CO. In H_2-TPR experiments, the peak β is mainly assigned to the reduction of Cu^+ to Cu^0, as a result, the lower reduction temperature (T_β) may lead to increase the activity; during the CO adsorption in situ FT-IR measurements, the increase and disappearance of Cu^+-CO species represent the progressive reduction of Cu^{2+} to Cu^+ and Cu^+ to Cu^0, therefore, the corresponding temperature to the maximum intensity of Cu^+-CO species (T_{max}) may be inversely proportional to the activity; the bigger the gradient of electronegativity between Cu and M (M = Ce, Zr, Sn, Ti), the easier Cu^+/Cu^0 can be obtained on the surface of the catalysts, which may be beneficial to the improvement of the activity. Interestingly, these properties are well in agreement with the activity (Fig. 11b). As a result, the activity of NO reduction by CO is related to the reducible property of the catalysts and the electronegativity of foreign metal cations. In addition, according to the results of NO adsorption and CO + NO co-adsorption in situ FT-IR, the activity may be related to the adsorption/desorption behavior. Through the above-mentioned comparative studies, we can find that the doping of Zr^{4+} is better than Sn^{4+} and Ti^{4+} for NO + CO reaction in the present work.

3.8. Possible reaction mechanism (schematic diagram) of NO reduction by CO

According to the above-mentioned characterizations, a possible reaction mechanism (schematic diagram) of NO reduction by CO under the current conditions is tentatively proposed to further understand the nature of this reaction (Fig. 12). Based on the CO and NO co-adsorption in situ FT-IR results, we can find that the reaction of NO reduction by CO over these $CuO/Ce_{0.67}M_{0.33}O_2$ (M = Zr^{4+}, Sn^{4+}, Ti^{4+}) catalysts passes the same reaction pathway, which is an Eley-Rideal (E-R) mechanism. In addition, the obtained results indicate that the doping of Zr^{4+} is better than Sn^{4+} and Ti^{4+} for NO + CO reaction in the present work. As a result, taking 04CuO/CZ as an example, the electrons can migrate from Ce^{4+} and Zr^{4+} to Cu^{2+} to generate Cu^+ at room temperature (25 °C) because the electronegativity of Cu is larger than those of Ce and Zr, which is supported by XPS and CO adsorption in situ FT-IR results. When exposing the catalyst to CO and NO mixture gases at 25 °C, NO molecules are preferentially adsorbed on the surface of the

catalyst to form several types of nitrite and nitrate species due to its unpaired electron, and this behavior inhibits the adsorption of CO species. Furthermore, the gaseous CO molecules can react with the adsorbed NO species to produce small amounts of N_2O, N_2 and CO_2 below 150 °C, which is in agreement with the catalytic activity/selectivity and CO + NO co-adsorption in situ FT-IR results. Increasing the temperature up to 150 °C leads the adsorbed NO species to be desorbed/transformed/decomposed, and then release the sites to adsorb CO. Simultaneously, some Cu^{2+} is reduced to Cu^{+} by CO in this process. Moreover, the gaseous NO molecules can react with the adsorbed CO species to produce more N_2O, N_2 and CO_2 below 250 °C. When the temperature further raising up to 250 °C, Cu^{+} can be reduced to Cu^{0} by CO. According to the measurement method of Cu dispersion [57], we can find that N_2O is able to oxidize Cu^{0} to Cu^{+} easily, indicating that Cu^{0} can promote the transformation of N_2O to N_2 efficiently. Therefore, a great number of N_2 and CO_2 are obtained during the temperature range of 250–325 °C.

4. Conclusions

The present work carried out a comparative study on the influence of different doped metal cations on structure, texture, reduction, and adsorption properties, as well as catalytic performance of $CuO/Ce_{0.67}M_{0.33}O_2$ ($M = Zr^{4+}$, Sn^{4+}, Ti^{4+}) catalysts for NO reduction by CO. Combining with the above-mentioned characterizations, the following conclusions can be obtained:

(I) The larger gradient of electronegativity between Cu and M (M = Ce, Zr, Sn, Ti) is beneficial to obtain Cu^{+}/Cu^{0} species, thus leading to an increase of activity for NO reduction by CO.
(II) 04CuO/CZ catalyst exhibits better catalytic performance than 04CuO/CS and 04CuO/CT, which may be related to its excellent reduction property and suitable adsorption/desorption behavior.
(III) The reaction of NO reduction by CO over these $CuO/Ce_{0.67}M_{0.33}O_2$ ($M = Zr^{4+}$, Sn^{4+}, Ti^{4+}) catalysts passes the same reaction pathway, which is an Eley-Rideal (E-R) mechanism.

Acknowledgments

The financial supports of the National Natural Science Foundation of China (No. 20973091), the National Basic Research Program of China (973 program, Nos. 2009CB623500, 2010CB732300) and Jiangsu Province Science and Technology Support Program (Industrial, BE2011167) are gratefully acknowledged.

References

[1] P. Araya, F. Gracia, J. Cortés, E.E. Wolf, Applied Catalysis B: Environmental 38 (2002) 77–90.
[2] P. Granger, L. Delannoy, J.J. Lecomte, C. Dathy, H. Praliaud, L. Leclercq, G. Leclercq, Journal of Catalysis 207 (2002) 202–212.
[3] H.O. Zhu, J.R. Kim, S.K. Ihm, Applied Catalysis B: Environmental 86 (2009) 87–92.
[4] C. Neyertz, M. Volpe, D. Perez, I. Costilla, M. Sanchez, C. Gigola, Applied Catalysis A:General 368 (2009) 146–157.
[5] V.I. Pârvulescu, P. Grange, B. Delmon, Catalysis Today 46 (1998) 233–316.
[6] Y.H. Hu, L. Dong, J. Wang, W.P. Ding, Y. Chen, Journal of Molecular Catalysis A: Chemical 162 (2000) 307–316.
[7] R.D. Zhang, W.Y. Teoh, R. Amal, B.H. Chen, S. Kaliaguine, Journal of Catalysis 272 (2010) 210–219.
[8] L.J. Liu, B. Liu, L.H. Dong, J. Zhu, H.Q. Wan, K.Q. Sun, B. Zhao, H.Y. Zhu, L. Dong, Y. Chen, Applied Catalysis B: Environmental 90 (2009) 578–586.
[9] Q. Yu, X.X. Wu, X.J. Yao, B. Liu, F. Gao, J.M. Wang, L. Dong, Catalysis Communications 12 (2011) 1311–1317.
[10] X.Y. Jiang, L.P. Lou, Y.X. Chen, X.M. Zheng, Catalysis Letters 94 (2004) 49–55.
[11] X.Y. Jiang, L.P. Lou, Y.X. Chen, X.M. Zheng, Journal of Molecular Catalysis A: Chemical 197 (2003) 193–205.
[12] M. Li, Z.G. Liu, Y.H. Hu, M.T. Wang, Colloids and Surfaces A: Physicochemical and Engineering Aspects 367 (2010) 17–23.
[13] Q. Yu, X.X. Wu, C.J. Tang, L. Qi, B. Liu, F. Gao, K.Q. Sun, L. Dong, Y. Chen, Journal of Colloid and Interface Science 354 (2011) 341–352.
[14] J.Z. Shyu, W.H. Weber, H.S. Gandhi, Journal of Physical Chemistry 92 (1988) 4964–4970.
[15] M. Yan, T. Mori, J. Zou, F. Ye, D.R. Ou, J. Drennan, Acta Materialia 57 (2009) 722–731.
[16] J.F. Chen, J.J. Zhu, Y.Y. Zhan, X.Y. Lin, G.H. Cai, K.M. Wei, Q. Zheng, Applied Catalysis A: General 363 (2009) 208–215.
[17] T. Yuzhakova, V. Rakić, C. Guimon, A. Auroux, Chemistry of Materials 19 (2007) 2970–2981.
[18] B. Bonnetot, V. Rakic, T. Yuzhakova, C. Guimon, A. Auroux, Chemistry of Materials 20 (2008) 1585–1596.
[19] L.J. Liu, Z.J. Yao, B. Liu, L. Dong, Journal of Catalysis 275 (2010) 45–60.
[20] J.L. Cao, Y. Wang, T.Y. Zhang, S.H. Wu, Z.Y. Yuan, Applied Catalysis B: Environmental 78 (2008) 120–128.
[21] W.T. Chen, K.B. Chen, M.F. Wang, S.F. Weng, C.S. Lee, M.C. Lin, Chemical Communications 46 (2010) 3286–3288.
[22] T. Baidya, A. Gupta, P.A. Deshpandey, G. Madras, M.S. Hegde, Journal of Physical Chemistry C 113 (2009) 4059–4068.
[23] J.L. Cao, Y. Wang, G. Sun, Z.Y. Zhang, Transition Metal Chemistry 36 (2011) 107–112.
[24] M.F. Luo, J. Chen, L.S. Chen, J.Q. Lu, Z.C. Feng, C. Li, Chemistry of Materials 13 (2001) 197–202.
[25] T.Y. Li, S.J. Chiang, B.J. Liaw, Y.Z. Chen, Applied Catalysis B: Environmental 103 (2011) 143–148.
[26] D.A. Andersson, S.I. Simak, N.V. Skorodumova, I.A. Abrikosov, B. Johansson, Physical Review B 76 (2007) 174119.
[27] B.M. Reddy, P. Bharali, P. Saikia, S.E. Park, M.W.E. van den Berg, M. Muhler, W. Grunert, Journal of Physical Chemistry C 112 (2008) 11729–11737.
[28] S. Tsushima, Journal of Physical Chemistry B 112 (2008) 13059–13063.
[29] Y. Liu, C. Wen, Y. Guo, G.Z. Lu, Y.Q. Wang, Journal of Physical Chemistry C 114 (2010) 9889–9897.
[30] T. Kobayashi, T. Yamada, K. Kayano, Applied Catalysis B: Environmental 30 (2001) 287–292.
[31] B.M. Reddy, A. Khan, P. Lakshmanan, M. Aouine, S. Loridant, J.C. Volta, Journal of Physical Chemistry B 109 (2005) 3355–3363.
[32] Y.H. Hu, L. Dong, M.M. Shen, D. Liu, J. Wang, W.P. Ding, Y. Chen, Applied Catalysis B: Environmental 31 (2001) 61–69.
[33] A. Martínez-Arias, M. Fernández-García, L.N. Salamanca, R.X. Valenzuela, J.C. Conesa, J. Soria, Journal of Physical Chemistry B 104 (2000) 4038–4046.
[34] J.R. McBride, K.C. Hass, B.D. Poindexter, W.H. Weber, Journal of Applied Physics 76 (1994) 2435–2441.
[35] K.S.W. Sing, D.H. Everett, R.A.W. Haul, L. Moscou, R.A. Pierotti, J. Rouquérol, T. Siemieniewska, Pure and Applied Chemistry 57 (1985) 603–619.
[36] X.W. Li, M.M. Shen, X. Hong, H.Y. Zhu, F. Gao, Y. Kong, L. Dong, Y. Chen, Journal of Physical Chemistry B 109 (2005) 3949–3955.
[37] P. Zimmer, A. Tschöpe, R. Birringer, Journal of Catalysis 205 (2002) 339–345.
[38] Z.G. Liu, R.X. Zhou, X.M. Zheng, Journal of Molecular Catalysis A: Chemical 267 (2007) 137–142.
[39] A.E. Nelson, K.H. Schulz, Applied Surface Science 210 (2003) 206–221.
[40] A. Pfau, K.D. Schierbaum, Surface Science 321 (1994) 71–80.
[41] S. Velu, K. Suzuki, C.S. Gopinath, H. Yoshida, T. Hattori, Physical Chemistry Chemical Physics 4 (2002) 1990–1999.
[42] F. Golestani-Fard, T. Hashemi, K.J.D. Mackenzie, C.A. Hogarth, Journal of Materials Science 18 (1983) 3679–3685.
[43] D. Shuttleworth, Journal of Physical Chemistry 84 (1980) 1629–1634.
[44] B.M. Reddy, P. Lakshmanan, A. Khan, Journal of Physical Chemistry B 108 (2004) 16855–16863.
[45] C.Z. Sun, J. Zhu, Y.Y. Lv, L. Qi, B. Liu, F. Gao, K.Q. Sun, L. Dong, Y. Chen, Applied Catalysis B: Environmental 103 (2011) 206–220.
[46] L.J. Liu, J.G. Cai, L. Qi, Q. Yu, K.Q. Sun, B. Liu, F. Gao, L. Dong, Y. Chen, Journal of Molecular Catalysis A: Chemical 327 (2010) 1–11.
[47] K.I. Hadjiivanov, Catalysis Reviews 42 (2000) 71–144.
[48] A. Martinez-Arias, J. Soria, J.C. Conesa, X.L. Seoane, A. Arcoya, R. Cataluna, Journal of the Chemical Society, Faraday Transactions 91 (1995) 1679–1687.
[49] X.Q. Cheng, A.M. Zhu, Y.Z. Zhang, Y. Wang, C.T. Au, C. Shi, Applied Catalysis B: Environmental 90 (2009) 395–404.
[50] Y.L. Fu, Y.C. Tian, P.Y. Lin, Journal of Catalysis 132 (1991) 85–91.
[51] M. Brandt, G. Zagatta, N. Böwering, U. Heinzmann, Surface Science 385 (1997) 346–356.
[52] V.P. Zhdanov, B. Kasemo, Surface Science Reports 29 (1997) 31–90.
[53] P. Granger, J.J. Lecomte, C. Dathy, L. Leclercq, G. Leclercq, Journal of Catalysis 175 (1998) 194–203.
[54] D. Li, Q. Yu, S.S. Li, H.Q. Wan, L.J. Liu, L. Qi, B. Liu, F. Gao, L.Y. Dong, Y. Chen, Chemistry- A European Journal 17 (2011) 5668–5679.
[55] T. Taniike, M. Tada, R. Coquet, Y. Morikawa, T. Sasaki, Y. Iwasawa, Chemical Physics Letters 443 (2007) 66–70.
[56] M. Tada, T. Taniike, Y. Iwasawa, Journal of Physical Chemistry C 111 (2007) 11663–11675.
[57] Z.L. Yuan, L.N. Wang, J.H. Wang, S.X. Xia, P. Chen, Z.Y. Hou, X.M. Zheng, Applied Catalysis B: Environmental 101 (2011) 431–440.